



## Research Paper

# Controlling the temperature build-up in electrode-sealed coin-shaped batteries via designing central heat dissipator

Asghar Aryanfar<sup>a,\*</sup>, Fadi Elias<sup>b</sup>, William A. Goddard III<sup>c</sup>

<sup>a</sup> Boğaziçi University<sup>1</sup>, Bebek, Istanbul, 34342, Turkey

<sup>b</sup> Lead Consult llc, Abu Dhabi, 47769, United Arab Emirates

<sup>c</sup> California Institute of Technology, 1200 E California Blvd, Pasadena, CA, 91125, USA

## ARTICLE INFO

Dataset link: [aryanfar@caltech.edu](mailto:aryanfar@caltech.edu)

## Keywords:

Thermal engineering  
Heat dissipation  
Heat generation  
Temperature profile  
Batteries  
Design

## ABSTRACT

Nowadays, the ever-increasing demand for the computational power in the calculators, watches and LED lights require higher consumption rate from their portable energy source, which is typically coin-shaped batteries. The required power generates and accumulates a large amount of heat, which is a critical safety concern due to flammability of the included organic electrolytes. When heat dissipation is minimal from the electrode surface, the packaging boundary remains the sole heat transfer medium. In such case, although the center carries a minimal real estate compared to the rest of the electrode surface, the heat gets trapped, due to having the lowest reach to the heat-dissipating boundaries. For this purpose, a central heat sink component is anticipated for the coin-shaped batteries and the temperature profile across the cell is analytically derived. Subsequently, the role of the sink thermal conductivity and its scale as well as the thermal conduction of the boundary on the formation of steady state temperature profile has been analyzed. More specifically, the location of the maximum temperature  $r_{max}$  and its value  $T_{max}$  is obtained and verified versus the extreme values of the thermal conductivities, the areal ratio of the heat sink, and the current density. The obtained results could be useful for the cost-effective design of the packaging materials (i.e. sustainable plastics and bio-degradable) with limited heat dissipation for the rechargeable batteries, particularly during the high power applications, in the presence of highly flammable electrolytes.

## 1. Introduction

Throughout the last few years, the technological advancement for the silicon-based portables has been trending at exponential rates [1]. Moreover, the environmental consequences of using traditional fossil fuels demands a new electric powered age with the introduction of hybrid and electric automotive industry [2–4]. Hence, it is imperative to equip such devices/vehicles with the highest possible energy density, to be usable over an extensive period [5,6]. In this regard, rechargeable lithium-based battery offers a clean and dense source of electric energy, which operates fundamentally via chemical reactions to generate electric current and posses the scalability and possibility to optimize comfort [7,8].

However, such exothermic reaction could lead to ignition, if not dissipated properly or when overcharged [9], and not only is the source of safety hazards [10], but also degrades the charge capacity and overall battery life [11]. In order to overcome such problem, several techniques have been developed and utilized, including forced convection [12], packaging design [13], calorimetry [14,

15], real time temperature monitoring [16,17], heat flux measurement [18], overcharge-analysis [19] and respective irregularities [20], inclusion of phase change materials (PCM) [4,21], bio-inspired micro-capsules [22], concentrated electrolytes [23], discharge method [24], capacity decay [25], developing machine learning method for estimating state of health [26], temperature range [27] and limit [28] for healthy operation, temperature-concentration [29] and temperature-resistance [30,31] and temperature-charge rate correlation [32], environmental temperature [33], and high Biot number applications [31, 34].

In particular, the design works on thermal management include, packing [35], designing heat-dissipating mini-channels [36], adding heat pipe [37], heat treatment for re-cycling [38], material selection and operational rate [39–41], packing allocation [42], designing temperature resilient electrolytes [43], adaptive heat management [44,45], larger-scale convection cooling [46] and adopting cost-effective and material-compatible geometrical design [47]. However,

\* Corresponding author at: California Institute of Technology, 1200 E California Blvd, Pasadena, CA, 91125, USA.

E-mail address: [aryanfar@caltech.edu](mailto:aryanfar@caltech.edu) (A. Aryanfar).

<sup>1</sup> a.k.a. Bosphorous University.

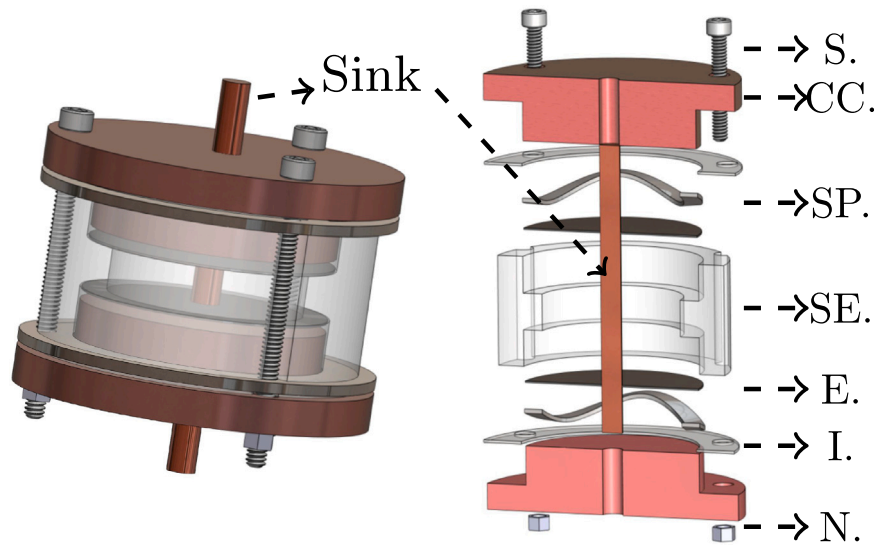


**Fig. 1.** The design for heat sink component to dissipate the heat generated in the central zone. Left: The packed battery illustrating the stuck-out heat sink component. Right: the exploded view of the components. S: screw, CC: current collector, SP: spring, SE: separator, E: electrode, I: insulator, N: nuts. When electrodes are thermally sealed, the dissipation of the generated heat occurs either through the center via the heat sink component (i.e. inner boundary:  $\kappa_I$ ) or the from the separator walls (i.e. outer boundary:  $\kappa_O$ ).

the overheating and ignition when warming up to the vicinity of the flash point temperature, remains a vital problem to overcome and optimize.

More specifically, the battery cells of coin (i.e. circular) geometry have been explored for heat generation using different discharge rates [48], utilizing infrared thermal imaging [49], micro-calorimetry [18], differential scanning calorimeter (DSC) and accelerating rate calorimeter (ARC) [50]. In particular, the heat treatment has been used for recycling of the active materials in coin cells illustrating the efficacy of heat on electrode [51]. However almost all the heat measurements have been for the entire battery as a whole and no local and on-spot measurements have been performed for predicting the spatial heat distribution of the coin shaped battery cells.

In this paper, we tackle into the most critical heat zone of the battery which is the center of the electrode [52] that carries the least heat dissipation rate due to its highest proximity from the boundaries [53]. Incorporating a rod of a limited conductivity as a heat sink, it can collect the central thermal energy and fork it out locally. Subsequently, we explore the role of the material type, current density and the relative scale of the heat sink component in the formation of the steady-state temperature profile. We establish the correlation of the materials, charging rate and geometry with the maximum temperature value, which helps to avoid the flash point of the electrolyte. The inclusion of the heat-sink stems the use of low heat-diffusivity sustainable packaging materials, that are recyclable and economical [54,55].

## 2. Methodology

The generation of heat during the battery operation is inevitable. In this regard, the operation is considered safe, when the built-up temperature always remains below the flash point of the incorporated electrolyte  $T_f$ . Such accumulation of heat occurs the most in the central zone due to being the most distant from the periphery. Since the center carries the smallest real estate, the limited generated heat could get dissipated out by designing a local heat sink component, as shown in Fig. 1. In this regard, while using the conductor candidates (i.e. metals) for packaging seems ideal for having the highest thermal conductivity, their electrical conductivity might hamper their use due to possibility of a short circuit. Therefore, the selection of the materials with limited conductivities (i.e. plastics) could be more cost-effective for packaging. Therefore, while inclusion of the metallic heat sink would require isolating membranes to separate it from the electrodes

and current collectors, the selection of the plastic material would be more design-effective, since no electrical insulation is required in packaging, and simple sealing would suffice. The list of candidate materials have been presented later in the Table 3.

During the operation, the oxidation and the reduction reactions in the electrode and counter electrode are endothermic and exothermic respectively with ideally the same rate. Hence, they neutralize each other for the net heat formation, and the remaining generated energy rate  $\dot{q}_{GEN}$  (i.e. heating up) will be due to the transport of the ions within the electrolyte medium. For the circular electrode with the radius  $R$ , the areal element would be  $dA = 2\pi r dr$  and the evolution of the temperature  $T(r, t)$  is obtained as [56]:

$$\frac{\partial T}{\partial t} = \alpha \left( \frac{\partial^2 T}{\partial r^2} + \frac{1}{r} \frac{\partial T}{\partial r} \right) + \frac{\dot{q}_{GEN}}{\rho c} \quad (1)$$

where  $r$  is the radial distance from the center ( $R_I \leq r \leq R_O$ ),  $t$  is the time,  $\alpha$ ,  $m$  and  $c$  are the heat diffusivity, mass and the specific heat capacity of the electrolyte. The rate of heat generation per unit area  $\dot{q}_{Gen}$  can be defined as the work of the drag force  $F_d$  on the charge carriers with the radius  $a$  as [57]:

$$\dot{q}_{GEN} = \frac{F_d l}{A l t} N \quad (2)$$

where  $l$ ,  $A$  and  $t$  are the inter-electrode distance, electrode surface area and time span for the ionic transition from one electrode to another. As well, the work of the drag force would be  $F_d = 6\pi\mu av$  due to Stokes law, where  $l$ ,  $t$  and  $v$  are the distance, the time and the velocity of ionic transfer in the inter-electrode space,  $N$  is Avogadro's number and  $\mu$  is the viscosity of the electrolyte. Having the current relationship as  $Q = It$  we re-write Eq. (2) as:

$$\dot{q}_{GEN} = 6\pi\mu a l N A \left( \frac{i}{Q} \right)^2 \quad (3)$$

where  $i$  is the current density,  $A$  is the electrode area and  $Q$  is the amount of the transferred charge. In the absence of the central heat sink, the generated heat typically needs to get transported to the boundaries and subsequently get dissipated there. However, the heat dissipation will be the hardest for the central zone and as a result more heat accumulation occurs in that region. In this regard, one could overcome with the temperature accumulation in the center by anticipating a heat-dissipating element as previously illustrated in Fig. 1.

**Table 1**  
Physical/Chemical parameters.

| Parameter               | Value          | Unit                                | Ref.     |
|-------------------------|----------------|-------------------------------------|----------|
| Heat capacity ( $c_p$ ) | 167            | J mol <sup>-1</sup> K <sup>-1</sup> | [58]     |
| Flash point ( $T_f$ )   | 134            | °C                                  | [59]     |
| $\kappa_E$              | 0.16           | W m <sup>-1</sup> K <sup>-1</sup>   | [60]     |
| $a$                     | 0.9            | Å                                   | [61]     |
| $R_I, R_O$              | 5,20           | mm                                  | Assigned |
| $l$                     | 3.2            | mm                                  |          |
| $Q$                     | 2 <sup>a</sup> | C                                   |          |
| $T_\infty$              | 298            | K                                   |          |
| $\delta$                | 0.1 $R_O$      | m                                   |          |

<sup>a</sup> Equivalent to 48 mAh charge.

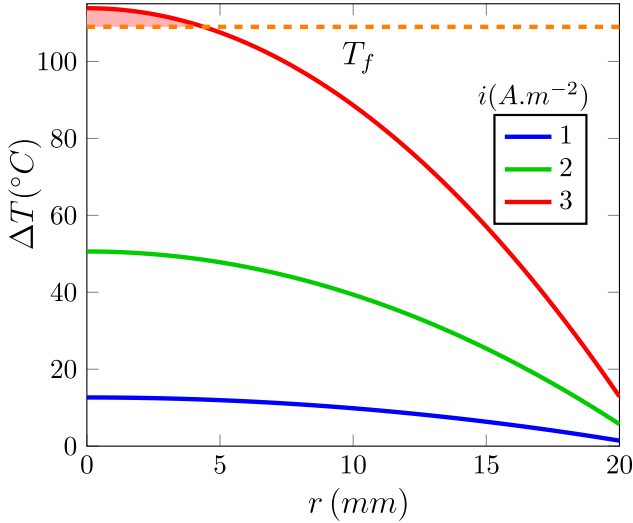


**Fig. 2.** The temperature build-up through the coin cell domain, with its critical value at the center ( $r = 0$ ).

### 2.1. Ordinary steady-state profile

From the temperature evolution relationship, given in Eq. (1), one can obtain the steady-state profile by setting  $\partial T / \partial t \approx 0$ , since there is no time dependency. For the electrolyte, noting  $\kappa_E = \rho c \alpha$ , one has:

$$\left( r \frac{\partial^2 T}{\partial r^2} + \frac{\partial T}{\partial r} \right) + \frac{\dot{q}_{GEN}}{\kappa_E} r = 0 \quad (4)$$

which could get re-written and integrated as:

$$\frac{dT}{dr} = -\frac{\dot{q}_{GEN}}{\kappa_E} \frac{r}{2} + \frac{C_1}{r} \quad (5)$$

$$T(r) = -\frac{\dot{q}_{GEN}}{4\kappa_E} r^2 + C_1 \ln(r) + C_2 \quad (6)$$

Since the temperature profile is symmetric from center, there will be no variation  $\left. \frac{dT}{dr} \right|_{r=0} \approx 0$ , hence  $C_1 = 0$ , and re-integrating leads to:

$$T = -\frac{\dot{q}_{GEN}}{\kappa_E} \frac{r^2}{4} + C_2 \quad (7)$$

The outer boundary could be considered as a thin ring with the thickness  $\delta$ . Thus, the heat passing through the electrolyte ( $\kappa_E$ ) will continue to pass through this medium ( $\kappa_O$ ). Hence:  $-\kappa_E \partial T / \partial r \Big|_{r=R_O} = \kappa_O \frac{T_O - T_\infty}{\delta}$ . For low temperature regime of operation, the ambient convection could get neglected and outer immediate temperature  $T_O$  will be same as the ambient temperature  $T_\infty$ . Therefore, the coefficient  $C_2$  is obtained as:

$$C_2 = \frac{\dot{q}_{GEN}}{2\kappa_O} R_O \delta + \frac{\dot{q}_{GEN}}{\kappa_E} \frac{R_O^2}{4} + T_\infty \quad (8)$$

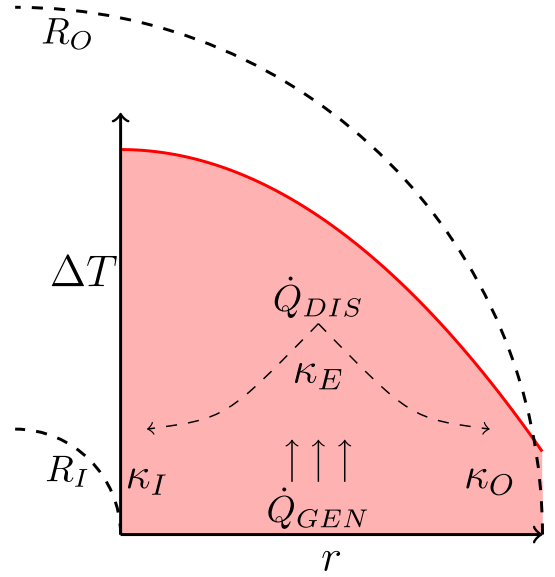


**Fig. 3.** Schematics of heat generation  $\dot{Q}_{GEN}$  and dissipation  $\dot{Q}_{DIS}$  throughout the electrolyte (i.e.  $\kappa_E$ ) and the central/peripheral (i.e.  $\kappa_I, \kappa_O$ ) boundaries of the half of the electrode cross-section.

Finally the temperature profile is attained as:

$$T = \frac{\dot{q}_{GEN}}{4\kappa_E} (R_O^2 - r^2) + \frac{\dot{q}_{GEN}}{2\kappa_O} R_O \delta + T_\infty \quad (9)$$

### 2.2. Inner or outer metallic boundary ( $\kappa_I \gg \kappa_E, \kappa_O$ or $\kappa_I, \kappa_E \ll \kappa_O$ )

As shown in the heat flow schematics in Fig. 3, the generated heat on the electrode surface passes initially through electrolyte (i.e.  $\kappa_E$ ) and later through the boundary material (inner heat sink  $\kappa_I$  or outer packaging material  $\kappa_O$ ) to get dissipated to the environment. Since these events occur consecutively (i.e. in series), either media could be limiting medium for heat transfer, given their respective thermal conductivities.

We have summarized the important possible case scenarios for the conductivity arrangements of the inner boundary  $\kappa_I$ , the electrolyte  $\kappa_E$  and outer boundary  $\kappa_O$  in the Table 2, where  $T_I$ ,  $T_O$  and  $T_\infty$  are the temperatures in the inner/outer boundaries and the ambient environment,  $l$  and  $\delta$  are the inter-electrode distance and the boundary thickness, and  $A_I = 2\pi R_I l$  and  $A_{ROD} = \pi R_I^2$  are the areas of the inner boundary and the cross-sectional area of the heat sink element (i.e. Rod) respectively.

For the case of metallic heat sink ( $\kappa_I \gg \kappa_E, \kappa_O$ ), the heat sink component will thermally short circuit with the environment where the temperatures become nearly identical. ( $T_I \approx T_\infty$ ). Adopting the respective boundary conditions for the inner temperature and the gradient of the outer temperature, given in the Table 2, and replacing into the Eqs. (5) and (6), one gets:

$$T = \frac{\dot{q}_{GEN}}{4\kappa_E} (R_I^2 - r^2) + \frac{\dot{q}_{GEN}}{4\kappa_E} \left( \frac{(R_O^2 - R_I^2) + \frac{2\kappa_E R_O \delta}{\kappa_O}}{\frac{\delta \kappa_E}{R_O \kappa_O} + \ln \left( \frac{R_O}{R_I} \right)} \right) \ln \left( \frac{r}{R_I} \right) + T_\infty \quad (10)$$

As well, for the outer metallic case ( $\kappa_O \gg \kappa_I, \kappa_E$ ), the metallic outer boundary will short circuit with the environment where the temperatures remain almost identical ( $T_O \approx T_\infty$ ). Henceforth, adopting the respective boundary conditions for outer temperature and the gradient of the inner temperature, given in the Table 2, and replacing into the

**Table 2**

All possible case scenarios for the thermal conductivity arrangements of the inner ( $\kappa_I$ ), electrolyte ( $\kappa_E$ ) and outer ( $\kappa_O$ ) media, with the respective appropriate boundary conditions.

| Section | Conductivity order                | Inner BC   | Outer BC   |
|---------|-----------------------------------|--|--|
| 2.2     | $\kappa_I \gg \kappa_E, \kappa_O$ | $T_\infty$   | $\kappa_E \frac{\partial T}{\partial r} \Big _{R_O} = \kappa_O \frac{T_O - T_\infty}{\delta}$  |
|         | $\kappa_I, \kappa_E \ll \kappa_O$ | $\kappa_E \frac{dT}{dr} \Big _{R_I} A_I = \kappa_I \frac{T_I - T_\infty}{l/2} A_{ROD}$                 | $T_\infty$   |
| 2.3     | $\kappa_I, \kappa_E, \kappa_O$    | $\kappa_E \frac{\partial T}{\partial r} \Big _{R_I} A_I = \kappa_I \frac{T_I - T_\infty}{l/2} A_{ROD}$ | $-\kappa_E \frac{\partial T}{\partial r} \Big _{R_O} = \kappa_O \frac{T_O - T_\infty}{\delta}$ |

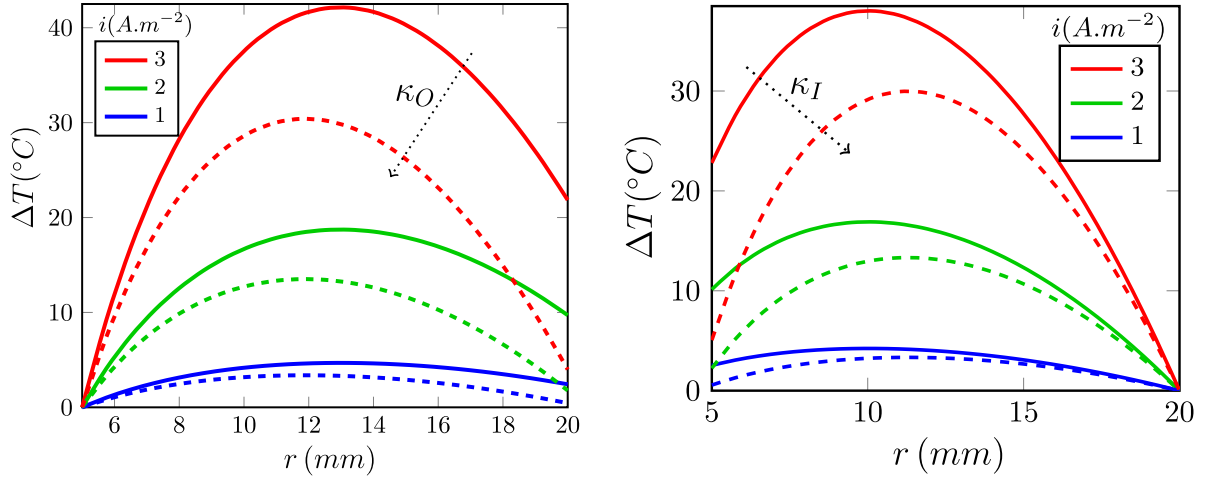


**Fig. 4.** Temperature profiles versus the inner and outer conductivities for (a) inner metallic and (b) outer metallic boundary condition. The solid to dashed lines represent the variation of the thermal conductivity of the plastic boundary from 0.08 W/m K to 0.49 W/m K.

Eqs. (5) and (6), one gets:

$$T = \frac{\dot{q}_{GEN}}{4\kappa_E} (R_O^2 - r^2) + \frac{\dot{q}_{GEN}}{4\kappa_E} \left( \frac{R_O^2 - R_I^2 + \frac{l R_I \kappa_E \hat{A}}{\kappa_I}}{\ln \left( \frac{R_O}{R_I} \right) + \frac{l \kappa_E \hat{A}}{2 \kappa_I R_I}} \right) \ln \left( \frac{r}{R_O} \right) + T_\infty \quad (11)$$

where  $\hat{A} = \frac{A_{ROD}}{A_I} = \frac{R_I}{2l}$  is the areal ratio of the inner boundary  $A_I = 2\pi R_I l$  to the rod  $A_{ROD} = \pi R_I^2$ . Figs. 4(a) and 4(b) visualize such temperature profiles versus the applied current density  $i$  and the variations in the limited conductivities of  $\kappa_I$  and  $\kappa_O$  respectively.

### 2.3. Inner/outer limited conductivities $\kappa_I, \kappa_E, \kappa_O$

For the last case in the Table 2, both boundaries pertain limited conductivities and the temperature profile will have an arched shape, which is suitable for exploring the location and magnitude of the maximum temperature, and has more versatile options for the materials selection in the boundary. Hence, the steady state evolution of the temperature profile is controlled by the dropping trend in the boundaries [62], and replacing them into the Eqs. (5) and (6) and simplifying, we arrive at:

$$T(r) = \frac{\dot{q}_{GEN}}{4\kappa_E} (R_I^2 - r^2) - \frac{\dot{q}_{GEN}}{\kappa_I} \frac{\hat{A} R_I l}{4} + T_\infty \quad (12)$$

$$+ \frac{\dot{q}_{GEN}}{2\kappa_E} \left( \frac{\frac{\hat{A} R_I \kappa_O l}{2\kappa_I} + R_O \delta + \frac{1}{2} \frac{\kappa_O}{\kappa_E} (R_O^2 - R_I^2)}{\frac{\hat{A} \kappa_O l}{2 R_I \kappa_I} + \frac{\delta}{R_O} + \frac{\kappa_O}{\kappa_E} \ln \left( \frac{R_O}{R_I} \right)} \right)$$

$$\times \left( \ln \left( \frac{r}{R_I} \right) + \frac{\hat{A} l}{2 R_I} \frac{\kappa_E}{\kappa_I} \right)$$

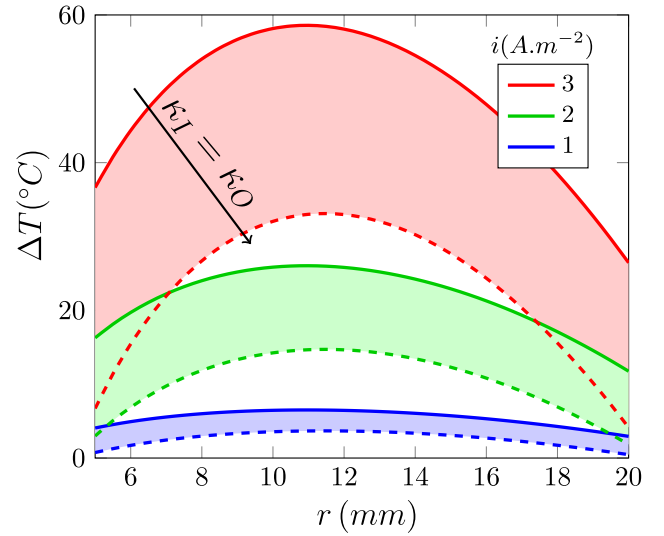


**Fig. 5.** Temperature profile for the two identical plastic materials used in the inner and outer boundaries. Solid:  $\kappa_I = \kappa_O = 0.08$  W/m K (EVA) and Dashed:  $\kappa_I = \kappa_O = 0.49$  W/m K (PE).

Fig. 5 illustrates the temperature profile for identical boundary materials (i.e.  $\kappa_I = \kappa_O$ ) versus the current density  $i$  based on the parameters given in the Table 1. As well, Fig. 8 (later in Results & Discussions) illustrates the variation of the steady-state temperature profile versus the ascending/descending trend in the imposed conductivity of the boundary. In this regard, while the extreme values



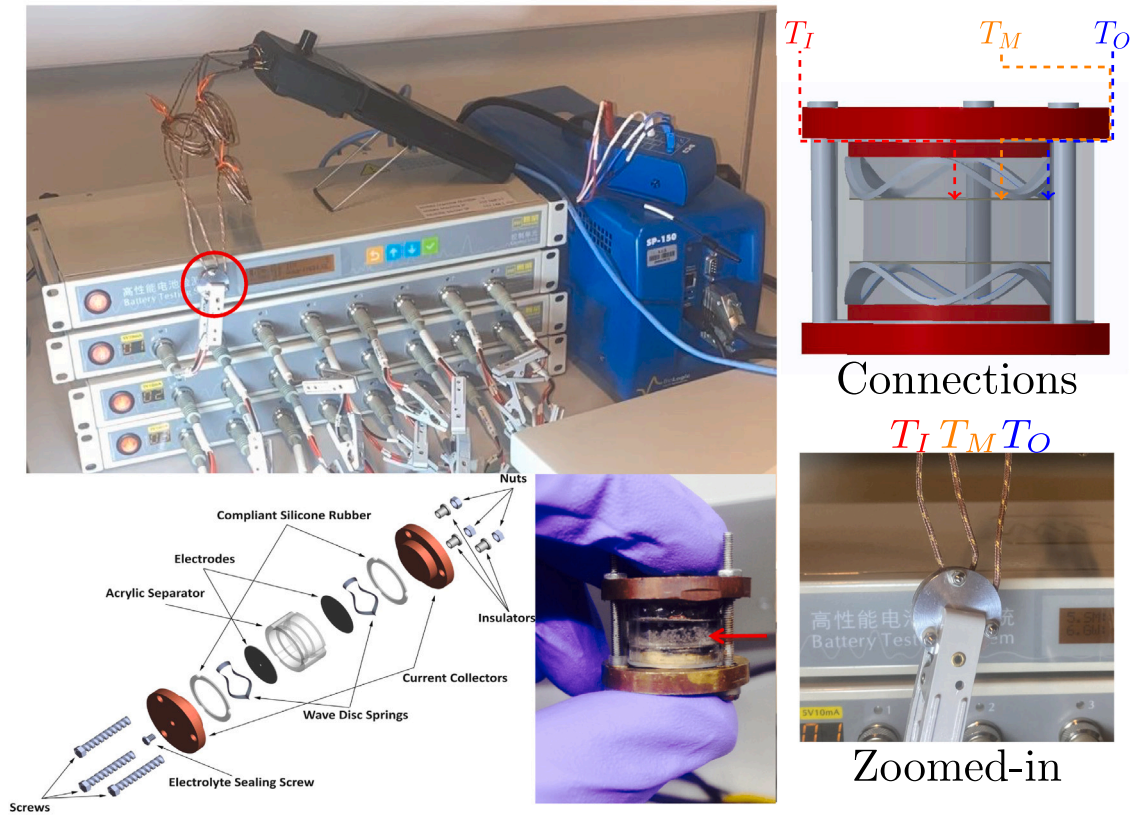


**Fig. 6.** The experimental setup. Top left: the coin-shaped cell (encircled) is connected to the potentiostat and the thermocouple wires are connected inside the cell. Top/Bottom right : The schematics and physical image of cell, illustrating the connection of thermocouple wires into the 3 distinct locations of inner center  $T_I$ , the midway through the center  $T_M$ , and the outer periphery  $T_O$ . Bottom left: Exploded view of the sandwich cell, detailing-out the individual components (no heat sink in the experimental measurement) [65]. Bottom center: Physical image of the coin-shaped cell, where the arrow shows the zone of heat generation and the microstructures [66].

**Table 3**

Candidate materials for the heat sink component (i.e. inner boundary:  $\kappa_I$ ) and packaging (i.e. outer boundary  $\kappa_O$ ).

| $\kappa_I, \kappa_O$                | Unit                            | Material  | Ref.    |
|-------------------------------------|---------------------------------|---|---------|
| 0                                   |                                 | Insulator   |         |
| 0.08                                |                                 | Ethylene-vinyl acetate (EVA)                      |         |
| 0.12                                |                                 | Polystyrene (PS)                                  |         |
| 0.18                                | $\text{W m}^{-1} \text{K}^{-1}$ | Polymethylmethacrylate (PMMA) CTherm <sup>a</sup> |         |
| 0.25                                |                                 | Teflon  |         |
| 0.49                                |                                 | Polyethylene (PE)                                 |         |
| $\sim 100 \text{ s (i.e. } \infty)$ |                                 | Metals (Short Circ.)                              | [63,64] |

<sup>a</sup> <https://ctherm.com/resources/newsroom/blog/the-thermal-conductivity-of-unfilled-plastics/>.

of conductivity belong to metals in  $\sim 100 \text{ s}$ , they are relatively far larger and are taken as  $\infty$ . The material candidates with the limited thermal conductivity  $\kappa$  are given in the Table 3 for either inner or outer dissipating boundaries. The upper and lower limits are 0.08, 0.49  $\text{W m}^{-1} \text{K}^{-1}$  (i.e. Ethylene-vinyl acetate (EVA) and Polyethylene (PE)) while more commonly-used materials (i.e. Polystyrene (PS), PMMA and Teflon) possess intermediate conductivity values of 0.12, 0.18 and 0.25  $\text{W m}^{-1} \text{K}^{-1}$  respectively.

### 3. Experimental

In order to explore the efficacy of the heat sink component on reducing the temperature, we have designed and fabricated coin shaped sandwich cells with thermally-sealed electrodes. The experimental setup has been shown in Fig. 6, top left.

The temperature measurements across the radial direction were performed in the locus of the center ( $T_I$ ), mid-radius ( $T_M$ ) and outside ( $T_O$ ) (Fig. 6, top/bottom right). Each cell is comprised of two disk electrodes, from lithium foil  $\text{Li}^\circ$  (anode) and the lithium cobalt oxide  $\text{LiCoO}_2$  (cathode), which are separated by the  $1 \text{ M LiPF}_6$  in  $\text{EC}$  electrolytic solution. The detailed compartments are shown in Fig. 6, bottom left, where the electrode-side thermal sealing was performed via inclusion of wave springs carrying the inert gas from the glovebox. The assembled physical appearance of the cell is shown in Fig. 6, bottom center. The preparation was executed as follows:

The lithium foil was acquired from Sigma Aldrich, 99.9% with the thickness of 0.38 mm and was placed into the glovebox (Changshu Tongrun Electronic Co.Ltd) with controlled moisture and oxygen ( $\text{H}_2\text{O}, \text{O}_2 < 1 \text{ ppm}$ ) and supplied by Argon. Subsequently, the punch (McMaster-Carr) was used to chop out several disk electrodes ( $d = \frac{9}{16}$ ) which were cleaned after via Dimethoxyethane (DME). Similarly, lithium cobalt oxide (Aldrich, 99.8% trace metals basis) was purchased and prepared as the counter electrode. The screws, insulators and nuts (shown in Fig. 1), were purchased from McMaster-carr. The current-collectors were precision-machined from an Aluminum plate (purchased from McMaster-carr) to the aligning dimensions with the screws/ insulators. Subsequently, the separator housing was first purchased as a PMMA plate from McMaster-carr. Afterwards the laser-cut was used to chop out circular rings. Consequently, circular housing was made with an intermediate diameter of the punched electrodes via the mill.

All the cells were initially placed on top of each other and were fastened via the screws on the periphery [65]. Afterwards, the screws were protected by the plastic insulators as sleeves to avoid the electrical connections between the facing current collectors. Three thermocouple

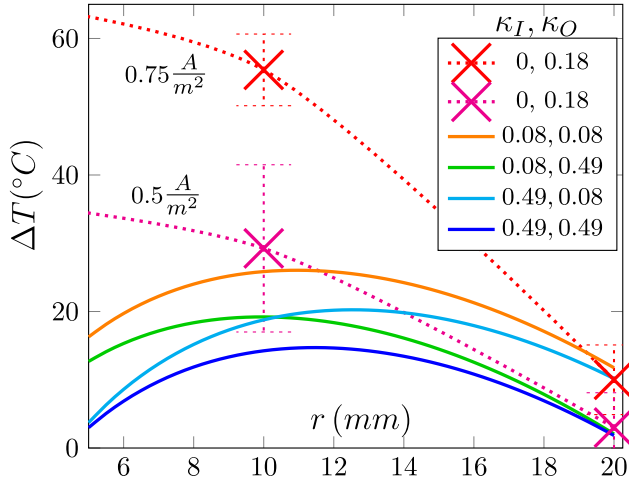


Fig. 7. Comparison of the measured temperature profile in the experiments, where heat sink is absent (dotted:  $\kappa_I := 0$ ), versus the calculated temperature profile in the presence of heat sink (solid:  $\kappa_I > 0$ ), for multitudes of the values for the inner and outer plastic materials with their specific thermal conductivities ( $\kappa_I$  and  $\kappa_O$ ). The experimental current densities are  $i = \{0.5, 0.75\} \text{ A m}^{-2}$  and the theoretical current density has been assigned as the  $i = 2 \text{ A m}^{-2}$ , which should have formed higher temperature, and obtaining lower temperature values even further proves the efficacy of the heat sink element.

wires were inserted in during the pre-assembled status and were connected to the center, mid-radius and outside locations to track the local temperature values (Fig. 6, bottom right). The metallic wave springs maintain the electrical connections while insulating the electrodes thermally. The thermal insulation from the electrode-side is in fact the extreme case scenario for trapping the heat in batteries, where the dissipation from the boundary becomes the most emphasized.

The electrolyte solution was fabricated by mixing lithium hexafluorophosphate  $\text{LiPF}_6$  (Aldrich, battery grade,  $\geq 99.99\%$ , trace metals basis) inside the ethylene carbonate  $\text{EC}$  (Aldrich, Anhydrous, 99%). Consequently, the electrolyte was injected via a syringe in the middle, which was fastened after.

Multiple cells were made, were taken out of the glovebox and were cycled in the multi-channel Neware potentiostat (5 mA – 10 V) with the current densities of  $\{0.5, 0.75\} \text{ A m}^{-2}$  at the rate of 4C for 20 cycles. Throughout each experiment, the temperature value started to increase until reaching a steady-state value after passing through a transient state. Afterwards, the maximum temperature values throughout the entire run were recorded, and their average and standard deviation were calculated. Fig. 7 visualizes and compares the obtained experimental values, versus the analytical temperature profile with similar parameters attained from Eq. (12). The comparison clearly shows the efficacy of the heat dissipator on mitigating the temperature build-up, particularly in the central zone, where the temperature would have been the highest.

#### 4. Results & discussion

Comparing the steady-state temperature profiles in Fig. 2 with Fig. 4(b), one notices that inclusion of even limited heat dissipator will greatly shift down the temperature distribution, including the maximum temperature  $T_{max}$ . The effectiveness of such limited-conductivity element, is mainly since the center carries a very small surface area, albeit being away from the outer boundaries. In fact, comparing the rate of formation of heat  $\dot{Q}_{GEN}$  with the rate of its dissipation  $\dot{Q}_{DIS}$  one notices that the former correlates with the area, while the latter correlates with the periphery. In other words:

$$\dot{Q}_{GEN} \sim r^2, \dot{Q}_{DIS} \sim r \quad (13)$$

which means that, assuming uniform generation of the heat across the electrode surface, moving toward the outer periphery, the likeliness of the temperature build-up should become higher. This is easily observable via comparing the temperature profiles in the 4(a) and 4(b), where the insulation of the outer periphery leads to higher temperature build-up. In this regard, an important measure is the maximum temperature value  $T_{max}$  which should not reach the critical state for safe operation, and is typically compared against the flash point  $T_f$  of the electrolyte.

The highest achievable temperature profile occurs during the steady-state regime of operation due to monotonous increase of the temperature from the initial transition. In the presence of the heat dissipator, the boundaries dissipate the temperature and therefore will have relatively lower temperature. Hence, one could find the location of the maximum temperature  $r_{max}$  by setting  $dT/dr = 0$  in Eq. (12), which yields:

$$r_{max} = \sqrt{\frac{\frac{R_I^2}{R_O^2} \frac{l}{R_I} \frac{\kappa_O}{\kappa_I} \frac{\hat{A}}{2} + \frac{\delta}{R_O} + \frac{1}{2} \frac{\kappa_O}{\kappa_E} \left(1 - \frac{R_I^2}{R_O^2}\right)}{\frac{l}{R_I} \frac{\kappa_O}{\kappa_I} \frac{\hat{A}}{2} + \frac{\delta}{R_O} + \frac{\kappa_O}{\kappa_E} \ln\left(\frac{R_O}{R_I}\right)} R_O \quad (14)$$

It is obvious that the location of maximum temperature  $r_{max}$  lies in between the inner and outer radii ( $R_I < r_{max} < R_O$ ). For the extreme case inner insulating dissipator ( $\kappa_I \rightarrow 0$ ) the first terms in the numerator and denominator of Eq. (14) become relatively significant. Hence, the location of maximum temperature  $r_{max}$  approaches to:

$$\lim_{\kappa_I \rightarrow 0} r_{max} \approx \sqrt{\frac{\frac{R_I^2}{R_O^2} \frac{l}{R_I} \frac{\kappa_O}{\kappa_I} \frac{\hat{A}}{2}}{\frac{l}{R_I} \frac{\kappa_O}{\kappa_I} \frac{\hat{A}}{2}}} R_O \approx R_I \quad (15)$$

which shows the highest temperature buildup in the inner radius  $R_I$ . As well, if both inner and outer materials are metallic, the conductivities become relatively extreme ( $\kappa_I \approx \kappa_O \rightarrow \infty$ ), and the last terms of Eq. (14) become significant. Therefore, the location of maximum temperature  $r_{max}$  would be:

$$r_{max} = \sqrt{\frac{R_O^2 - R_I^2}{2 \ln\left(\frac{R_O}{R_I}\right)}} \quad (16)$$

This is consistent with the previous study on the metallic boundaries [67]. Finally, for the extreme case of outer insulating material  $\kappa_O \rightarrow 0$ , the second terms of Eq. (14) in the numerator and denominator become significant and the location of the maximum temperature  $r_{max}$  becomes:

$$r_{max} \approx \sqrt{\frac{\frac{\delta}{R_O}}{\frac{\delta}{R_O}}} R_O \approx R_O \quad (17)$$

which shows the highest temperature buildup in the outer radius  $R_O$ . Such transition in the location of the maximum temperature value  $r_{max}$  versus the relative variations in inner  $\kappa_I$  (i.e. heat sink) and outer  $\kappa_O$  (i.e. outer packaging) thermal conductivities is visualized in Fig. 8, where the increase in the inner conductivity  $\kappa_I$  and decrease in the outer conductivity, moves the location of maximum temperature outward from inner  $R_I$  to outer  $R_O$  radius. Additionally, it is evident that the minimum critical temperature occurs when both the boundary materials are metallic, with the highest rate of heat dissipation.

Looking further into the variation of the temperature profile versus the respective inner/outer conductivities  $\kappa_I, \kappa_O$ , it is evident that even the smallest inner thermal conductivity  $\kappa_I$  will have a significant role on reducing the temperature value, compared with having substantial conductivity in the outer region. In other words, the central heat dissipator acts as a bridge for cutting the span of heat dissipation from

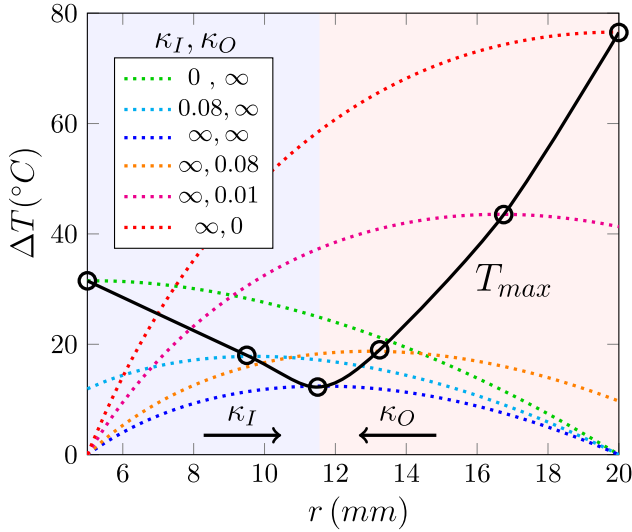


Fig. 8. Tracking the established maximum temperature  $T_{max}$ , versus the variation in the inner  $\kappa_I$  and outer  $\kappa_O$  conductivities. The insulating and metallic boundaries are characterized by 0 and  $\infty$  thermal conductivities.

2R to R which significantly reduce the maximum temperature. This shows the importance of the heat transport as a global effect within the cell domain versus the heat dissipation in the boundaries (i.e. local effect).

As well, while the relationship for the maximum cell temperature  $T_{max}$  is obtained by calculating the steady-state temperature value  $T(r)$  (Eq. (12)) in the location of the maximum temperature  $r_{max}$  (Eq. (14)) as:

$$T_{max} = \frac{\dot{q}_{GEN}}{4\kappa_E} R_I^2 \left( \frac{f_1}{f_3} + \frac{f_2}{f_3} \left( \ln \left( \frac{f_2}{f_3} \right) + \hat{A} \frac{l}{R_I} \frac{\kappa_E}{\kappa_I} \right) \right) - \frac{\hat{A}}{4} \frac{\dot{q}_{GEN}}{\kappa_I} R_I l + T_{\infty} \quad (18)$$

where the coefficients  $f_1$ ,  $f_2$  and  $f_3$  are obtained as:

$$\begin{cases} f_1 = \ln \left( \frac{R_O}{R_I} \right) - \frac{1}{2} \left( \frac{R_O^2}{R_I^2} - 1 \right) \\ f_2 = \frac{\hat{A}}{2} \frac{l}{R_I} \frac{\kappa_E}{\kappa_I} + \frac{1}{2} \left( \frac{R_O^2}{R_I^2} - 1 \right) \\ f_3 = \frac{\hat{A}}{2} \frac{l}{R_I} \frac{\kappa_E}{\kappa_I} + \ln \left( \frac{R_O}{R_I} \right) \end{cases} \quad (19)$$

which is function of both geometrical and physical parameters.

Scale-wise, one could assess its relevance to the relative rod-to-cell scale which is inherent in the areal ratio  $\hat{A} = \frac{A_{ROD}}{A_I} = \frac{R_I}{2l}$  in its extreme values. The lowest efficiency of the heat dissipator would be for the thinnest ( $R_I \downarrow$ ) and longest inter-electrode length ( $l \uparrow$ ), where  $\hat{A}$  turns negligible and the maximum temperature difference  $\Delta T_{max} = T_{max} - T_{\infty}$  becomes:

$$\lim_{\hat{A} \rightarrow 0} \Delta T_{max} = \frac{\dot{q}_{GEN}}{4\kappa_E} \left( R_I^2 + \frac{(R_O^2 - R_I^2)}{2 \ln \left( \frac{R_O}{R_I} \right)} \ln \left( \frac{\left( \frac{R_O^2}{R_I^2} - 1 \right)}{\ln \left( \frac{R_O}{R_I} \right)^{2e}} \right) \right) \quad (20)$$

Vice versa, the highest dissipation occurs, if the areal ratio  $\hat{A}$  becomes significantly large, and in the limit the maximum temperature difference  $\Delta T_{max}$  turns into:

$$\begin{aligned} \lim_{\hat{A} \rightarrow \infty} \Delta T_{max} &= -\hat{A} \frac{\dot{q}_{GEN}}{\kappa_I} \frac{R_I l}{4} + \frac{\dot{q}_{GEN}}{4\kappa_I} R_I (\hat{A} l) \\ &= 0 \end{aligned} \quad (21)$$

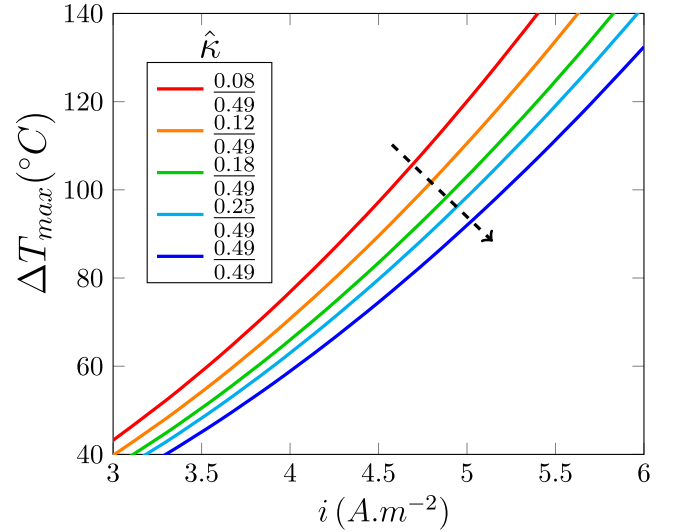


Fig. 9. The maximum temperature  $T_{max}$  versus the imposed current density  $i$  for different inner-to-outer conductivity ratio of  $\hat{\kappa} = \frac{\kappa_I}{\kappa_O}$ .

which means that the dissipator has significantly larger scale than the cell and the temperature remains in balance with the environment.

Material-wise, Fig. 9 shows the variation of the maximum temperature  $\Delta T_{max}$  versus the current density  $i$  (which correlates with the generated heat  $\dot{q}_{GEN}$ ), where the increase in the conductivity ratio ( $\hat{\kappa} = \kappa_I/\kappa_O$ ) tends to shift down the maximum temperature  $\Delta T_{max}$ .

Needless to mention that the generated heat in this study is assumed to be generated from the cations and the role of the anions are neglected. As well, the heat dissipation was attributed only through the boundaries, and the other thermal dissipation sources such as the electrode surface in the sealed electrode is neglected. The future steps include computing for the transient heat generation, its distribution across the electrode surface and the resulted build-up of the temperature profile.

Finally, the idea of the heat sink component is to connect the central zone of the battery, as the most critical for accumulating temperature, to the environment, which bridges down the span of the temperature profile. In other words, the heat sink element acts as a type of a boundary, and its small area is proportional to the involved real estate in the center. Hence, the heat dissipation design with sink component should be applicable for other types of batteries, where its efficacy would correlate with the involved geometry.

## 5. Conclusions

We have elaborated on a new design for the effective heat dissipation from the most critical site (i.e. central zone) of the coin batteries, with the limited peripheral heat depletion. We have included a heat sink element which carries the heat out from in/out plane directions and reduces-down the temperature distribution across the electrode domain. As well, we have characterized the efficacy of heat dissipation versus thermal conductivity and the relative scale of the heat sink component. The location of the maximum temperature and its value is analytically derived versus the geometry of the cell and the thermal conductivities of the electrolyte, peripheral boundary and the heat sink element. Finally, the effect of the extreme values of the heat sink areal ratio  $\hat{A}$  is analyzed for obtaining the maximum temperature. The developed design and subsequent characterization could be utilized for effective temperature control of the batteries of coin-geometry in any scale, for maintaining the safe performance at high power rates. This could get particularly useful for engineering stationary applications, where there is a wide range of options for material-selection due to versatility in the design and sustainable operation.



## Nomenclature

$l$  : inter-electrode distance (m)  
 $\dot{q}_{GEN}$  : rate of heat generation per area ( $\text{J m}^{-2} \text{s}^{-1}$ )  
 $N$  : Avogadro's number ( $6 \times 10^{23} \text{ atoms mol}^{-1}$ )  
 $T_{\infty}$  : ambient temperature (K)  
 $\kappa_I$  : inner boundary thermal conductivity ( $\text{W m}^{-1} \text{K}^{-1}$ )  
 $\kappa_O$  : Outer boundary thermal conductivity ( $\text{W m}^{-1} \text{K}^{-1}$ )  
 $\kappa_{PC}$  : Polycarbonate thermal conductivity ( $\text{W m}^{-1} \text{K}^{-1}$ )  
 $\rho_{PC}$  : Polycarbonate density ( $\text{kg m}^{-3}$ )  
 $t$  : time (s)  
 $v$  : velocity of ionic transfer ( $\text{m s}^{-1}$ )  
 $F_d$  : Drag force on the charge carriers (N)  
 $\dot{A}$  : areal ratio of the rod surface to the outer boundary ([])  
 $R_I$  : inner radius of cell (m)  
 $R_O$  : outer radius of cell (m)  
 $\mu$  : viscosity of LiPF<sub>6</sub> (mpa s)  
 $a$  : ionic radius of Li<sup>+</sup> (Å)  
 $i$  : current density ( $\text{A m}^{-2}$ )  
 $A$  : electrode area ( $\text{m}^2$ )  
 $Q$  : amount of charge (C)  
 $\alpha$  : thermal diffusivity of LiPF<sub>6</sub> ( $\text{m}^2 \text{s}^{-1}$ )  
 $T$  : absolute temperature (K)  
 $r$  : radial spatial coordinate (m)  
 $c$  : specific heat ( $\text{J kg K}^{-1}$ )  
 $T_f$  : flash point (K)  
 $\delta r$  : radial segmentation (m)  
 $\delta t$  : time segmentation (s)  
 $\delta$  : the boundary thickness (m)

## Declaration of competing interest

The authors declare that they have no known competing financial interests or personal relationships that could have appeared to influence the work reported in this paper.

## Data availability

The raw data for producing the results in this manuscript are freely available upon request from the corresponding author at [aryanfar@caltech.edu](mailto:aryanfar@caltech.edu).

## References

- [1] John Shalf, The future of computing beyond Moores law, *Phil. Trans. R. Soc. A* 378 (2166) (2020) 20190061.
- [2] Ahmad A. Pesaran, Battery thermal models for hybrid vehicle simulations, *J. Power Sources* 110 (2) (2002) 377–382.
- [3] Chester G Motloch, Jon P Christophersen, Jeffrey R Belt, Randy B Wright, Gary L Hunt, Raymond A Sutula, Tien Duong, Thomas J Tartamella, Harold J Haskins, Ted J Miller, High-power battery testing procedures and analytical methodologies for HEV's, *SAE Trans.* (2002) 797–802.
- [4] Gi-Heon Kim, Ahmad Pesaran, Battery thermal management design modeling, *World Electr. Veh. J.* 1 (1) (2007) 126–133.
- [5] Jeff Tollefson, Charging up the future: a new generation of lithium-ion batteries, coupled with rising oil prices and the need to address climate change, has sparked a global race to electrify transportation, *Nature* 456 (7221) (2008) 436–441.
- [6] Dwayne N Fry, David E Holcomb, John K Munro, Lester C Oakes, MJ Matson, Compact Portable Electric Power Sources, Technical Report, Oak Ridge National Lab.(ORNL), Oak Ridge, TN (United States), 1997.
- [7] George Crabtree, Elizabeth Kócs, Lynn Trahey, The energy-storage frontier: Lithium-ion batteries and beyond, *Mrs Bull.* 40 (12) (2015) 1067–1078.
- [8] Peter J. Hall, Euan J. Bain, Energy-storage technologies and electricity generation, *Energy Policy* 36 (12) (2008) 4352–4355.
- [9] Pius Victor Chombo, Yossapong Laoonual, A review of safety strategies of a Li-ion battery, *J. Power Sources* 478 (2020) 228649.
- [10] Dongxu Ouyang, Mingyi Chen, Que Huang, Jingwen Weng, Zhi Wang, Jian Wang, A review on the thermal hazards of the lithium-ion battery and the corresponding countermeasures, *Appl. Sci.* 9 (12) (2019) 2483.
- [11] Bahman Shabani, Manu Biju, Theoretical modelling methods for thermal management of batteries, *Energies* 8 (9) (2015) 10153–10177.
- [12] Gholamreza Karimi, Xianguo Li, Thermal management of lithium-ion batteries for electric vehicles, *Int. J. Energy Res.* 37 (1) (2013) 13–24.
- [13] X.M. Xu, R. He, Review on the heat dissipation performance of battery pack with different structures and operation conditions, *Renew. Sustain. Energy Rev.* 29 (2014) 301–315.
- [14] Xuan Liu, Stanislav I Stolarov, Matthew Denlinger, Alvaro Masias, Kent Snyder, Comprehensive calorimetry of the thermally-induced failure of a lithium ion battery, *J. Power Sources* 280 (2015) 516–525.
- [15] Yangyang Fu, Song Lu, Kaiyuan Li, Changchen Liu, Xudong Cheng, Heping Zhang, An experimental study on burning behaviors of 18650 lithium ion batteries using a cone calorimeter, *J. Power Sources* 273 (2015) 216–222.
- [16] Panding Wang, Xinyi Zhang, Le Yang, Xingyu Zhang, Meng Yang, Haosen Chen, Daining Fang, Real-time monitoring of internal temperature evolution of the lithium-ion coin cell battery during the charge and discharge process, *Extreme Mech. Lett.* 9 (2016) 459–466.
- [17] Hewu Wang, Yajun Zhang, Weifeng Li, Zhenhai Gao, Baodi Zhang, Minggao Ouyang, Experimental study on the cell-jet temperatures of abused prismatic Ni-rich automotive batteries under medium and high states of charge, *Appl. Therm. Eng.* 202 (2022) 117859.
- [18] Chen Liang, Lihua Jiang, Shuliang Ye, Zhaoyu Wang, Zesen Wei, Qingsong Wang, Jinhua Sun, Precise in-situ and ex-situ study on thermal behavior of LiNi<sub>1</sub>/3Co<sub>1</sub>/3Mn<sub>1</sub>/3O<sub>2</sub>/graphite coin cell: From part to the whole cell, *J. Energy Chem.* 54 (2021) 332–341.
- [19] Chen Liang, Lihua Jiang, Shuliang Ye, Jinhua Sun, Qingsong Wang, Comprehensive analysis on dynamic heat generation of LiNi<sub>1</sub>/3Co<sub>1</sub>/3Mn<sub>1</sub>/3O<sub>2</sub> coin cell under overcharge, *J. Electrochem. Soc.* 166 (14) (2019) A3369.
- [20] Fiona C Strohbridge, Bernardo Orvananos, Mark Croft, Hui-Chia Yu, Rosa Robert, Hao Liu, Zhong Zhong, Thomas Connolly, Michael Drakopoulos, Katsuyo Thornton, et al., Mapping the inhomogeneous electrochemical reaction through porous LiFePO<sub>4</sub>-electrodes in a standard coin cell battery, *Chem. Mater.* 27 (7) (2015) 2374–2386.
- [21] Fenfang Chen, Rui Huang, Chongming Wang, Xiaoli Yu, Huijun Liu, Qichao Wu, Keyu Qian, Rohit Bhagat, Air and PCM cooling for battery thermal management considering battery cycle life, *Appl. Therm. Eng.* 173 (2020) 115154.
- [22] Zhenhai Gao, Shun Rao, Tianyao Zhang, Fei Gao, Yang Xiao, Longfei Shali, Xiaoxu Wang, Yadan Zheng, Yiyuan Chen, Yuan Zong, et al., Bioinspired thermal runaway retardant capsules for improved safety and electrochemical performance in lithium-ion batteries, *Adv. Sci.* 9 (5) (2022) 2103796.
- [23] Junxian Hou, Languang Lu, Li Wang, Atsushi Ohma, Dongsheng Ren, Xuning Feng, Yan Li, Yalun Li, Issei Ootani, Xuebing Han, et al., Thermal runaway of lithium-ion batteries employing LiN (SO<sub>2</sub>F) 2-based concentrated electrolytes, *Nature Commun.* 11 (1) (2020) 5100.
- [24] Yin Zhang, John N. Harb, Performance characteristics of lithium coin cells for use in wireless sensing systems: Transient behavior during pulse discharge, *J. Power Sources* 229 (2013) 299–307.
- [25] Sung Park, Andreas Savvides, Mani B. Srivastava, Battery capacity measurement and analysis using lithium coin cell battery, in: ISLPED'01: Proceedings of the 2001 International Symposium on Low Power Electronics and Design (IEEE Cat. No. 01TH8581), IEEE, 2001, pp. 382–387.
- [26] Jianyu Zhang, Wei Lu, Sparse data machine learning for battery health estimation and optimal design incorporating material characteristics, *Appl. Energy* 307 (2022) 118165.
- [27] Ahmad Pesaran, Andreas Vlahinos, Thomas Stuart, et al., Cooling and preheating of batteries in hybrid electric vehicles, in: 6th ASME-JSME Thermal Engineering Joint Conference, Citeseer, 2003, pp. 1–7.
- [28] Andreas Vlahinos, Ahmad A. Pesaran, Energy efficient battery heating in cold climates, *SAE Trans.* (2002) 826–833.
- [29] Yonghuang Ye, Yixiang Shi, Ningsheng Cai, Jianjun Lee, Xiangming He, Electro-thermal modeling and experimental validation for lithium ion battery, *J. Power Sources* 199 (2012) 227–238.
- [30] S.S. Zhang, K. Xu, T.R. Jow, The low temperature performance of Li-ion batteries, *J. Power Sources* 115 (1) (2003) 137–140.
- [31] Nicolas Damay, Christophe Forgez, Marie-Pierre Bichat, Guy Friedrich, Thermal modeling of large prismatic LiFePO<sub>4</sub>/graphite battery. Coupled thermal and heat generation models for characterization and simulation, *J. Power Sources* 283 (2015) 37–45.
- [32] Meng Xu, Zhuqian Zhang, Xia Wang, Li Jia, Lixin Yang, Two-dimensional electrochemical-thermal coupled modeling of cylindrical LiFePO<sub>4</sub> batteries, *J. Power Sources* 256 (2014) 233–243.
- [33] Tugce Yuksel, Jeremy J. Michalek, Evaluation of the effects of thermal management on battery life in plug-in hybrid electric vehicles, 2012.
- [34] Rajib Mahamud, Chanwoo Park, Spatial-resolution, lumped-capacitance thermal model for cylindrical Li-ion batteries under high Biot number conditions, *Appl. Math. Model.* 37 (5) (2013) 2787–2801.
- [35] H Fayaz, Asif Afzal, AD Samee, Manzoore Elahi M Soudagar, Naveed Akram, MA Mujtaba, RD Jilte, Md Islam, Ümit Ağbulut, C Ahammed Saleel, et al., Optimization of thermal and structural design in lithium-ion batteries to obtain energy efficient battery thermal management system (BTMS): a critical review, *Arch. Comput. Methods Eng.* (2021) 1–66.



- [36] Wei Li, Xiongbin Peng, Mi Xiao, Akhil Garg, Liang Gao, Multi-objective design optimization for mini-channel cooling battery thermal management system in an electric vehicle, *Int. J. Energy Res.* 43 (8) (2019) 3668–3680.
- [37] Mao-Sung Wu, K.H. Liu, Yung-Yun Wang, Chi-Chao Wan, Heat dissipation design for lithium-ion batteries, *J. Power Sources* 109 (1) (2002) 160–166.
- [38] Yue Yang, Emenike G Okonkwo, Guoyong Huang, Shengming Xu, Wei Sun, Yinghe He, On the sustainability of lithium ion battery industry—A review and perspective, *Energy Storage Mater.* 36 (2021) 186–212.
- [39] Rui Liu, Jixin Chen, Jingzhi Xun, Kui Jiao, Qing Du, Numerical investigation of thermal behaviors in lithium-ion battery stack discharge, *Appl. Energy* 132 (2014) 288–297.
- [40] Kaiwei Chen, Heat Generation Measurements of Prismatic Lithium Ion Batteries (Master's thesis), University of Waterloo, 2013.
- [41] Kazuo Onda, Takamasa Ohshima, Masato Nakayama, Kenichi Fukuda, Takuto Araki, Thermal behavior of small lithium-ion battery during rapid charge and discharge cycles, *J. Power Sources* 158 (1) (2006) 535–542.
- [42] Parisa Amiribavandpour, Weixiang Shen, Daobin Mu, Ajay Kapoor, An improved theoretical electrochemical-thermal modelling of lithium-ion battery packs in electric vehicles, *J. Power Sources* 284 (2015) 328–338.
- [43] Marco-Tulio F Rodrigues, Kaushik Kalaga, Hemtej Gullapalli, Ganguli Babu, Arava Leela Mohana Reddy, Pulickel M Ajayan, Hexagonal boron nitride-based electrolyte composite for Li-ion battery operation from room temperature to 150°C, *Adv. Energy Mater.* 6 (12) (2016) 1600218.
- [44] M Shadman Rad, DL Danilov, M Baghalha, M Kazemeini, PHL Notten, Adaptive thermal modeling of Li-ion batteries, *Electrochim. Acta* 102 (2013) 183–195.
- [45] Zhonghao Rao, Shuangfeng Wang, A review of power battery thermal energy management, *Renew. Sustain. Energy Rev.* 15 (9) (2011) 4554–4571.
- [46] Xiongwen Zhang, Xin Kong, Guojun Li, Jun Li, Thermodynamic assessment of active cooling/heating methods for lithium-ion batteries of electric vehicles in extreme conditions, *Energy* 64 (2014) 1092–1101.
- [47] Patrick Bonnick, J.R. Dahn, A simple coin cell design for testing rechargeable zinc-air or alkaline battery systems, *J. Electrochem. Soc.* 159 (7) (2012) A981.
- [48] Hans Giel, David Henriques, George Bourne, Torsten Markus, Investigation of the heat generation of a commercial 2032 (LiCoO<sub>2</sub>) coin cell with a novel differential scanning battery calorimeter, *J. Power Sources* 390 (2018) 116–126.
- [49] SERDAR Altin, E Altundag, EMİNE Altin, SEBAHAT Altundag, Improved battery performance of silicon modified Na<sub>0.67</sub>Fe<sub>0.5</sub>Mn<sub>0.5</sub>O<sub>2</sub> and its structural and electrochemical properties: An investigation of infrared thermal imaging, *J. Energy Storage* 41 (2021) 102979.
- [50] Humberto Joachin, Thomas D. Kaun, K. Zaghib, J. Prakash, Electrochemical and thermal studies of LiFePO<sub>4</sub> cathode in lithium-ion cells, *ECS Trans.* 6 (25) (2008) 11.
- [51] Sanjay Pindar, Nikhil Dhawan, Recycling of discarded coin cells for recovery of metal values, *Miner. Eng.* 159 (2020) 106650.
- [52] Moo-Yeon Lee, Namwon Kim, Jae-Hyeong Seo, Mahesh Suresh Patil, Thermal abuse behavior of the LIR2450 micro coin cell battery having capacity of 120 mAh with internal short circuit by penetrating element, *Symmetry* 12 (2) (2020) 246.
- [53] Dong Hyup Jeon, Seung Man Baek, Thermal modeling of cylindrical lithium ion battery during discharge cycle, *Energy Convers. Manage.* 52 (8–9) (2011) 2973–2981.
- [54] Naoki Nitta, Feixiang Wu, Jung Tae Lee, Gleb Yushin, Li-ion battery materials: present and future, *Mater. Today* 18 (5) (2015) 252–264.
- [55] Fereshteh Samimi, Aziz Babapoor, Mohammadmehdi Azizi, Gholamreza Karimi, Thermal management analysis of a li-ion battery cell using phase change material loaded with carbon fibers, *Energy* 96 (2016) 355–371.
- [56] Theodore L Bergman, Theodore L Bergman, Frank P Incropera, David P Dewitt, Adrienne S Lavine, *Fundamentals of Heat and Mass Transfer*, John Wiley & Sons, 2011.
- [57] Robert W. Fox, Alan T. McDonald, John W. Mitchell, Fox and McDonald's Introduction to Fluid Mechanics, John Wiley & Sons, 2020.
- [58] I.A. Vasilev, D.M. Korkhov, I.B. Rabinovich, M.S. Sheiman, V.P. Nistratov, Heat capacity and thermodynamic functions for propylene carbonate, *Termodin. Org. Soedin.* (1976) 21–26.
- [59] Steffen Hess, Margret Wohlfahrt-Mehrens, Mario Wachtler, Flammability of Li-ion battery electrolytes: flash point and self-extinguishing time measurements, *J. Electrochem. Soc.* 162 (2) (2015) A3084.
- [60] M. Tuliszkza, F. Jaroszyk, M. Portalski, Absolute measurement of the thermal conductivity of propylene carbonate by the AC transient hot-wire technique, *Int. J. Thermophys.* 12 (5) (1991) 791–800.
- [61] Robert D. Shannon, Revised effective ionic radii and systematic studies of interatomic distances in halides and chalcogenides, *Acta Crystallogr. Sect. A* 32 (5) (1976) 751–767.
- [62] Yaman Yener, Sadik Kakaç, *Heat Conduction*, CRC Press, 2018.
- [63] J.E. Graves, E. Latvytė, Alan Greenwood, N.G. Emekwuru, Ultrasonic preparation, stability and thermal conductivity of a capped copper-methanol nanofluid, *Ultrason. Sonochem.* 55 (2019) 25–31.
- [64] Liang Chen, Shuangtao Chen, Yu Hou, Understanding the thermal conductivity of diamond/copper composites by first-principles calculations, *Carbon* 148 (2019) 249–257.
- [65] Asghar Aryanfar, Daniel Brooks, Boris V. Merinov, William A. Goddard III, Agustín J. Colussi, Michael R. Hoffmann, Dynamics of lithium dendrite growth and inhibition: Pulse charging experiments and Monte Carlo calculations, *J. Phys. Chem. Lett.* 5 (10) (2014) 1721–1726.
- [66] Asghar Aryanfar, Tao Cheng, Agustín J. Colussi, Boris V. Merinov, William A. Goddard III, Michael R. Hoffmann, Annealing kinetics of electrodeposited lithium dendrites, *J. Chem. Phys.* 143 (13) (2015) 134701.
- [67] Asghar Aryanfar, Fadi Elias, William A. Goddard, Enhancing the thermal dissipation in batteries via inclusion of central heat sink, *J. Electrochem. Energy Convers. Storage* 21 (2) (2024).